Int. J. Heat Mass Transfer. Vol. 34, No. 3, pp. 589–600, 1991
Printed in Great Britain

0017–9310/91 $3.00+0.00

Pressure drop characteristics of heat exchangers consisting of arrays of diamond-shaped pin fins

E. M. SPARROW
Department of Mechanical Engineering, University of Minnesota, Minneapolis, MN 55455, U.S.A.

and

V. B. GRANNIS
Occupational Health and Environmental Safety Division, 3M Company, St. Paul, MN 55144, U.S.A.

(*Received* 27 *February* 1990 *and in final form* 14 *May* 1990)

Abstract—A broad-ranging investigation encompassing complementary experimentation and numerical simulation is performed to determine the pressure drop characteristics of arrays of diamond-shaped pin fins. The array geometrical parameters S_T/W and S_L/W, respectively, range from 1.15 to 2.00 and from 1.00 to 2.00, where W is the maximum fin width and S_T and S_L the transverse and longitudinal spacings. The investigated fins have forward-facing vertex angles of either 45 or 90 deg. The Reynolds number, based on the maximum fin width and the maximum fluid velocity, ranges from about 20 to 2200. From the experiments, highly accurate data for selected arrays are obtained for the per-row pressure drop, for the combined entrance and exit losses, and for the length of the hydrodynamic development region. The per-row pressure drop data served as a standard of comparison for the predictions of the numerical simulations, which are performed using a finite-element code applied to the periodic fully developed regime. The thus-validated simulation model is employed to generate results for a wide range of geometrical conditions. To facilitate their application to design, the numerically determined per-row pressure drop results are correlated by compact algebraic equations (equations (12)–(15)).

1. INTRODUCTION

THE INITIAL motivation for this research on arrays of diamond-shaped pin fins was the design of an air-to-air heat exchanger flown on space shuttle flight STS-34 which was launched on 18 October 1989. This heat exchanger served to cool the electronic equipment and other apparatus heat sources in a 3M Company experiment carried aboard the shuttle. The exchanger consisted of two independent arrays of diamond-shaped pin fins, with one array extending normal to one face of a baseplate and the other array extending normal to the other face of the baseplate. The fins were fabricated integral to the baseplate by starting with an aluminum plate of uniform thickness and milling a pattern of deep grooves into each face.

Power and noise level constraints limited the size of the fans that could be used to drive the airflow, which meant that pressure drop considerations were of major importance. In reviewing the literature on pin fin arrays, it was discovered that there was no available knowledge base for the pressure drop characteristics of diamond-shaped pin fin arrays (and similarly for the heat transfer characteristics of such arrays). The research program now to be described was undertaken to provide a knowledge base for the pressure drop characteristics.

The overall research plan encompassed a synergistic combination of experimentation and numerical simulation. The first step was to obtain highly accurate experimental data for the pressure drop characteristics of selected diamond-shaped pin fin arrays. These data were then used to establish the range of validity of numerical predictions from computer simulations carried out for these cases. Once the numerical simulation had been validated, it was employed to obtain pressure drop characteristics for additional diamond-shaped pin fin arrays beyond those of the experiments (i.e. other pitches and layouts). As a final step, the entire body of numerical results was generalized by curve fits to facilitate their application to the design of arrays the characterizing parameters of which lay within the range of the simulations.

The reporting of the overall investigation has been subdivided into two parts according to function and focus and in order to stay within journal length limitations. The present paper is practice-oriented. It conveys a full description of the experiments, the experimental results, the comparisons with the numerical simulations, and the generalizing curve fits. A second paper [1] will focus on the numerical simulations and on a full presentation of the numerical results.

For the experimental part of the research, an apparatus was designed and fabricated to facilitate highly accurate measurements of the axial pressure distribution in diamond-shaped pin fin arrays. The fins were fabricated to close tolerances by an injection molding process and were installed in a duct in an equilateral-triangular array consisting of 20 rows, with 12 fins in each row. Two diamond-shaped fin

NOMENCLATURE

A_{min}	minimum free flow area
D^*	porosity-based characteristic length, equations (7) and (8)
f	per-row friction factor, equation (10)
H	fin height
L	streamwise length of diamond-shaped pin fin
$\dot{m}$	mass flow rate
N	number of rows
p_{down}	pressure downstream of the array
p_{up}	pressure upstream of the array
$\Delta p_{ent/exit}$	combined entrance and exit pressure losses, equation (4)
Δp_{row}	per-row pressure drop in the periodic fully developed regime
Re	Reynolds number, $\rho V_{max} W/\mu$
Re^*	Reynolds number, $\rho V_{max} D^*/\mu$
S_L	longitudinal center-to-center spacing between fins
S_T	transverse center-to-center spacing between fins
V_{max}	average velocity in the minimum free flow area
W	maximum transverse width of diamond-shaped pin fin.

Greek symbols

μ	viscosity
ξ	per-row dimensionless pressure coefficient, equation (1)
ρ	density
ϕ	dimensionless combined entrance and exit pressure losses, equation (5).

geometries were employed, one with a 45-deg vertex angle and the other with a 90-deg vertex angle. For each fin geometry, the array was characterized by dimensionless transverse and longitudinal spacings (based on the maximum fin width) of 2.00×1.73.

The experiments were conducted over a Reynolds number range covering two orders of magnitude (from about 20 to 2200 for Re based on the maximum fin width and the maximum velocity). Over the span of the investigated Reynolds numbers, the flow in the array extended from the laminar regime into the transition to turbulence. Air was the working fluid in all the experiments. Results obtained from the experiments included the fully developed per-row pressure coefficients for the arrays, the entrance lengths, and the entrance and exit losses.

The numerical simulations utilized the FIDAP finite-element code in conjunction with a periodic fully developed model of the flow field. The flow was assumed steady and laminar, with constant properties.

As already noted, the authors were unable to find any prior information on the pressure drop (or heat transfer) characteristics of diamond-shaped pin fin arrays in the published literature. There is, on the other hand, a very considerable literature on the pressure drop characteristics of circular-tube pin fin arrays. Among these, the most encompassing presentations of results are those of Zukauskus [2] and of Gaddis and Gnielinski [3].

2. EXPERIMENTS

2.1. *Experimental apparatus*

The experimental apparatus was an open-circuit airflow system operated in the suction mode. Along its path of flow, air from the laboratory room passed successively through the test section, flow metering station, control valve, and blower, from which it was discharged into a service corridor.

The test section was a rectangular duct having a 7.62×7.62 cm square cross section (3.000×3.000 in.) and an overall length of 62.2 cm (24.5 in.). It consisted of three functional zones. The initial zone spanned a length of 25.4 cm (10 in.) downstream from the inlet. It served as a hydrodynamic development section and to dissipate any effects of possible flow separation at the inlet. The second zone, an axial length of approximately 11.4 cm (4.5 in.), housed the diamond-shaped pin fin arrays the pressure drop characteristics of which were to be determined. The final zone, a length of duct of 25.4 cm (10 in.), allowed free expansion of the flow leaving the array and also served to buffer the array from any effects of an abrupt contraction which occurred at the downstream end of the test section.

The aforementioned functional zones are clearly in evidence in the photograph of the test section that is presented in Fig. 1. The pin fin array and the internal surfaces of the duct are visible through the transparent upper wall of the duct. In the photograph, the open inlet of the test section is on the right while the square-to-circular transition configuration at the duct exit is shown on the left.

The side and lower walls of the test section duct were fabricated from aluminum, while the upper wall was fabricated from clear polycarbonate. The respective thicknesses of the side and upper walls and of the lower wall were 1.27 cm (1/2 in.) and 1.91 cm (3/4 in.). Longitudinal recesses were cut adjacent to the edges of the upper and lower walls to facilitate dovetail mating with the side walls, thereby ensuring the strength and stability of the structure. To guard against leakage, O-ring material was laid in longitudinal grooves that had been milled into the top and

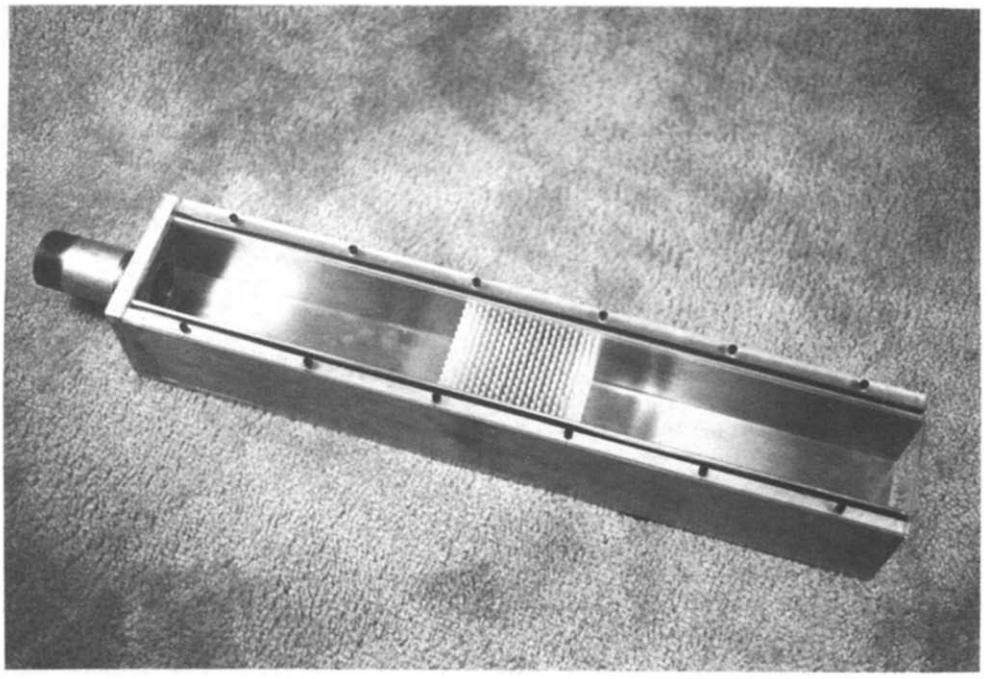

FIG. 1. Photograph of the test section.

bottom edges of the side walls. The assembled duct was held together by suitably positioned screws. All of the milling operations were performed with a numerically controlled milling machine.

The downstream end of the duct was capped by a square plate of aluminum into which a centered circular hole had been machined and threaded. A short length of circular pipe (i.d. $\cong 4$ cm (1.6 in.)) was inserted into the hole to consummate the square-to-circular transition of the flow path.

To fix the position and alignment of the individual pin fins, a patterned array of 230 holes was drilled into the upper face of the lower wall of the test section. The locating and drilling of the holes was numerically controlled, with the drilling operation followed by a reaming operation. The function of each such hole was to receive and positively position a cylindrical shank which extended downward from the base of each pin fin. Each hole was 0.1994 cm (0.0785 in.) in diameter and 1.524 cm (0.600 in.) deep.

Two distinct diamond-shaped pin fin geometries were utilized in the experiments, and these are illustrated in Fig. 2. As seen there, the parameter which characterizes the fin shape is the forward (or rear) vertex angle, for which values of 45 and 90 deg were chosen. For a given value of the vertex angle, it remains to specify either the transverse width W (as seen by the oncoming flow) or the axial length L in order to fix the size of the fin planform. The width W was used for this purpose. Furthermore, W was also used in the representation of the dimensionless pitches of the array, i.e. S_T/W and S_L/W, where S_T and S_L are the actual transverse and longitudinal pitches.

For the experiments, it was decided to use common values of S_T/W and S_L/W for the two types of fin geometries (i.e. for the two vertex angles). Furthermore, to enable the same baseplate (i.e. same pattern of fin–shank seat holes) to be utilized for both arrays, the pitches S_T and S_L were chosen to be common. As a consequence, the same width W was used for the two fin geometries.

The fins were fabricated with $W = 0.3175$ cm (0.125 in.). The corresponding axial lengths L for the 45- and 90-deg vertex angle fins are 0.7621 cm (0.302 in.) and 0.3175 cm (0.125 in.). In order to minimize end effects resulting from the finite height of the fins, Gaddis and Gnielinski [3] recommend that the fin height H be at least 10 times the fin diameter (for circular fins). This criterion was more than fulfilled in the present apparatus by making the fin height $H = 24W$, so that $H = 7.620$ cm (3.000 in.).

The diamond-shaped pin fins were manufactured by an injection molding process. Since more than 460 fins were needed for the experiments, this method of manufacture was judged to be the most efficient and

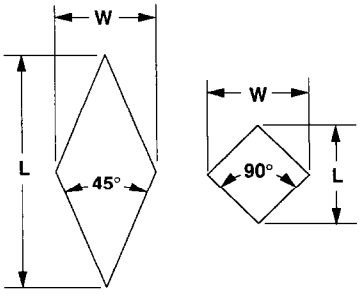

FIG. 2. Diamond-shaped pin fin geometries.

cost-effective approach for obtaining accurate and consistent reproductions of the desired fin geometry. A 30% glass-filled ABS plastic was used as the molding material. This type of plastic provided both excellent dimensional tolerances and good structural rigidity.

The desired fin geometries were first machined into carbon electrodes. The carbon electrodes were then used in an electrical discharge machine to burn the shape into a steel mold. The surface of the mold was hand polished to a finish of less than 16 micro-in. Ra. The 45- and 90-deg vertex angle fins were molded side-by-side in a family mold. The mold cavities were gated at the end away from the shank so the plastic would flow the entire length of the pin fin. The cooling lines in the mold ran along the length of the part. The gating at the end of the part and the cooling line placement are important to minimize possible warp of the plastic part upon ejection. Because 460 parts is a relatively small number compared with commercial injection molding practice, a relatively long cycle time of 30 s was allowable and desired to give the plastic ample time to cool in the mold, which further minimized the possible warp. The care taken in molding was rewarded by the consistent dimensional precision of the pin fins. No dimension of any part varied by 0.00254 cm (0.001 in.) from nominal, and there was only 0.00254 cm (0.001 in.) of warp along the entire fin height.

To help in the attainment of flow conditions which more closely approximated those in an array of infinite width, half-width pin fins were positioned adjacent to the side walls of the duct in alternate rows. The half-width fins were readily molded in half the mold, with one of the mold-cavity plates replaced by a flat plate. With this arrangement, the parting plane of the mold was the same as the symmetry plane of the pin fin. The achieved dimensional tolerances for the half-width fins were identical to those for the full-width fins.

The fully assembled arrays utilized in the experiments are pictured schematically in Figs. 3(a) and (b), which correspond respectively to the 45- and 90-deg vertex angle fins. As seen there, the fins are positioned in a staggered, equilateral-triangular pattern. Both arrays are characterized by the dimensionless pitches $S_T/W = 2.00$ and $S_L/W = 1.732$. The arrays consist of 20 rows, with 12 fins in each row. This number of fins per row exceeds the number 10 suggested by Gaddis and Gnielinski [3] for the avoidance of significant side-wall effects. Further reduction of possible side-wall effects was achieved by the use of half-width fins adjacent to the duct side walls.

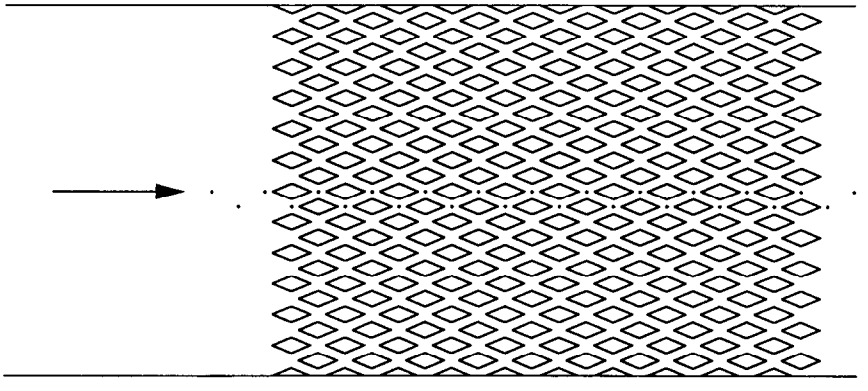

FIG. 3(a). Fully assembled array consisting of 45-deg vertex angle pin fins.

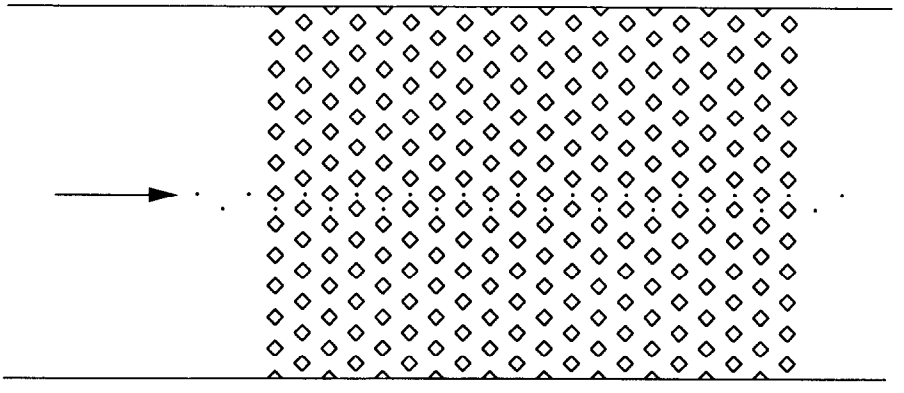

FIG. 3(b). Fully assembled array consisting of 90-deg vertex angle pin fins.

The full-width fins were assembled by pressing their shanks into the seat holes provided in the lower wall of the duct. The half-width fins were glued to the side walls.

Further inspection of Fig. 3 reveals the distinctly different character of the two arrays. In particular, the array with the 90-deg vertex angle fins is much more open than the array with the 45-deg vertex angle fins.

In addition to showing the layout of the arrays, Fig. 3 also displays the locations of pressure taps used in the determination of the pressure distributions. The tap locations are designated by small circle symbols. The taps were installed in the lower wall of the test section, as will soon be described. As seen in the figure, there is a tap in each row within the array. In addition, taps were provided both upstream and downstream of the array in order to facilitate the determination of the overall pressure drop. Although not shown, there were seven taps upstream of the array and six taps downstream of the array. All told, there were 33 pressure taps.

The taps are numbered sequentially from 1 to 33, with numbers increasing in the downstream direction. The numbering sequence is illustrated in Fig. 4. Tap number 1 was located on the longitudinal centerline of the duct, 3.43 cm (1.35 in.) from the inlet. Taps 1–5 are lined up along the centerline and separated by a spacing of 5.08 cm (2 in.). Taps 5–29 are positioned such that their longitudinal spacing is equal to the longitudinal spacing (0.5499 cm (0.2165 in.)) of the successive rows of the array. The taps in the array, numbers 8–27, are centered between the diamond-shaped pin fins, resulting in a staggered pattern.

This pattern was also used in positioning taps 5–7 and 28 and 29, which are adjacent to but outside of the array. The spacing returns to a 5.08-cm (2-in.), in-line pattern for taps 29–33.

The pressure tap holes were positioned and drilled using numerically controlled tooling. The tap hole opening that faced the airflow in the duct was made as small as possible, 0.0889 cm (0.035 in.) in diameter, to minimize the disturbance of the flow. Each tap hole was completed by a larger hole drilled into the lower wall from below. A short length of stainless steel tubing was inserted into the enlarged portion of the tap hole, and a plastic tube was slipped over the exposed end of the stainless steel.

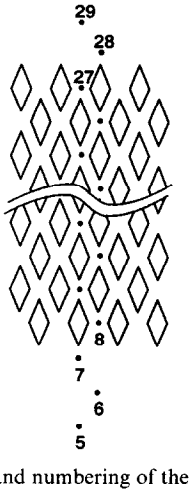

FIG. 4. Layout and numbering of the pressure taps.

The plastic tubes from the pressure taps were connected to the valved inlet ports of a pressure selector switch. In turn, the exit port of the selector switch was connected via a plastic tube to one terminal of a Baratron capacitance-type pressure meter (the other terminal was left open to ambient pressure). All told, three Baratron meters were used to measure the pressure distributions—two with a maximum pressure sensing capability of 1 Torr and one with a maximum capability of 10 Torr. The respective resolutions of the meters are 10^{-5} and 10^{-4} Torr. The pressure-related voltage outputs from the Baratron meters were read and time-averaged by a digital voltmeter. The procedures employed in processing the time-averages will be described shortly.

The primary flowmeter for determining the mass flow rate of the air was a calibrated orifice plate situated in a pipe with properly sized upstream and downstream lengths. Two different plates (i.e. different orifice hole diameters) were used to cover different portions of the flow rate range. The orifice pressures were read with 10 and 100 Torr Baratron pressure meters.

At the very low flows, a calibrated rotameter was used to measure the flow rates. The valving arrangement was such that the orifice meter and the rotameter were in series, thereby enabling comparisons between the two meters.

2.2. *Experimental procedure*

As a prelude to the collection of the data to be reported later, a number of verification data runs were made. In one such run, performed at a flow rate where both the orifice meter and the rotameter provided accurate data, the respective mass flows measured by the two instruments were 0.1478 and 0.1474 $lb_m\ s^{-1}$, an agreement within 0.3%. For another test, two successive data runs were made at identical flow rates, but with different 1 Torr pressure meters used to measure the respective pressure distributions. The resulting per-row pressure drops from the two meters differed by no more than 1%. In still another verification run, a 10 Torr meter and a 100 Torr meter were used to measure the pressure drop across the orifice plate. The two meters agreed to within 0.1%.

It was standard practice in all data runs to time-average the pressure signals at each tap to eliminate random fluctuations. As already noted, the digital voltmeter which received the output of the Baratron pressure meter averaged the signal over a 3 s interval. At each tap, a succession of such 3 s averages were recorded and subsequently averaged. The number of successive measurements depended on the degree of

steadiness of the pressure at the tap, with the criterion being that the average of the 3 s averages be independent of further contributions to the averaging process. It was found that 5, 10, and 20 readings per tap were appropriate for the low, intermediate, and high Reynolds number ranges, with corresponding averaging times of 15, 30, and 60 s.

The apparatus was initially set up for the array of 45-deg diamond-shaped pin fins. Once the Reynolds number range for this case had been covered, the 45-deg fins were removed and replaced with the 90-deg vertex angle fins, after which the same Reynolds number range was traversed. Each data run was conducted under steady-state conditions, with all components fully warmed up and stabilized.

2.3. *Data reduction*

The first step in the data reduction for each run was the execution of the averaging process that was described in the foregoing, subsequent to which the pressure distribution was graphed and examined. It is well established that after the fluid has traversed the first several rows of a tube bank, a periodic fully developed regime is established whereby the flow pattern is precisely repeated from row to row. In addition, in the periodic regime, the pressure drop per row is constant, so that the pressure differences between successive taps separated by an axial distance S_L are the same. As a consequence, it is expected that the measured axial pressure distributions would display a linear portion, and this expectation was fulfilled in all of the data runs.

The onset of the linear regime depends on the Reynolds number and the fin geometry, as will be documented later. However, for all cases, the pressure data between taps 12 and 24 were definitely linear. These data were used to fit a least-square straight line, the slope of which is the fully developed pressure drop per row Δp_{row}.

It is standard practice to report the pressure drop per row in terms of a dimensionless pressure coefficient defined as

$$\xi = \Delta p_{row}/\tfrac{1}{2}\rho V_{max}^2. \tag{1}$$

Here, the density ρ was evaluated from the perfect gas law at the average pressure in the array and at the measured (uniform) air temperature. The quantity V_{max} is the average velocity in the minimum free flow area A_{min}. In any row

$$A_{min} = 12[H(S_T - W)] \tag{2}$$

where $H(S_T - W)$ is the minimum free flow area between adjacent tubes in a given row, and there are 12 tubes in a row. Then

$$V_{max} = \dot{m}/\rho A_{min}. \tag{3}$$

The mass flow rate $\dot{m}$ was determined by conventional processing of the pressure data at the orifice or by converting the rotameter scale reading from standard to operating conditions.

The measurement of pressures upstream and downstream of the array enabled the evaluation of the entrance and exit losses. These losses are defined here as the difference between the actual overall pressure drop and the pressure drop in an array where the flow is fully developed in all rows. Therefore

$$\Delta p_{ent/exit} = (p_{up} - p_{down}) - N(\Delta p_{row}). \tag{4}$$

In this equation, p_{up} and p_{down} are the pressures upstream and downstream of the array, Δp_{row} is the fully developed pressure drop per row, and N is the number of rows ($= 20$ in the present experiments). The difference between $(p_{up} - p_{down})$ and $N(\Delta p_{row})$ is very much smaller than the quantities being differenced, thereby resulting in a loss of significant figures. A dimensionless form of the entrance and exit losses was evaluated as

$$\phi = \Delta p_{ent/exit}/\tfrac{1}{2}\rho V_{max}^2. \tag{5}$$

The experimentally determined pressure drop results were parameterized by the Reynolds number defined as

$$Re = \rho V_{max} W/\mu \tag{6}$$

in which the maximum fin width W was used as the characteristic dimension. The other characterizing parameters were the dimensionless transverse and longitudinal pitches S_T/W and S_L/W, the values of which were fixed for the experiments as 2.00 and 1.73.

3. EXPERIMENTAL RESULTS

All told, pressure distributions were measured in 29 final data runs. These runs covered the range of Reynolds numbers from 20 to about 2200 for both of the investigated diamond-shaped pin fin arrays. A representative sample of the pressure distributions is presented in Figs. 5(a)–(c) and 6(a)–(c), respectively, for the 45- and 90-deg vertex angle fins. The (a), (b), and (c) parts of these figures are for Reynolds numbers of approximately 45, 380, and 2200.

In each figure, the pressure at the successive taps is plotted as a function of the tap number. The tap locations that are situated within the array are 8–27, with lower-numbered taps in the test-section duct upstream of the array and higher-numbered taps in the test-section duct downstream of the array. In each figure, the pressure has been referred to its value in the test-section duct upstream of the array, so that all pressure distributions begin with an ordinate value of zero.

The downsloping straight line which appears in each figure is a least-squares fit of the pressure data between (and including) taps 12 and 24. As noted earlier, a linear pressure variation was achieved in this range for all of the data runs. In each figure, the aforementioned least-squares straight line was extended throughout the entire array to enable deviations from it to be readily identified.

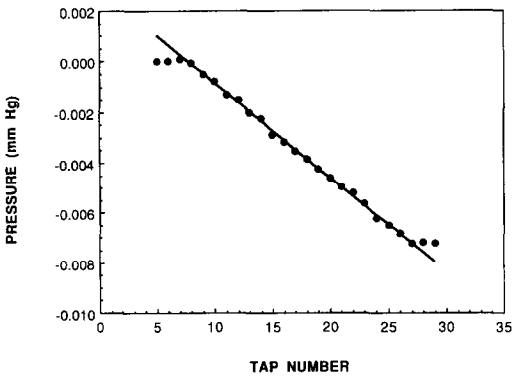

FIG. 5(a). Measured pressure distribution in a 45-deg vertex angle pin fin array for $Re = 43.5$. $S_T/W = 2.00$ and $S_L/W = 1.73$.

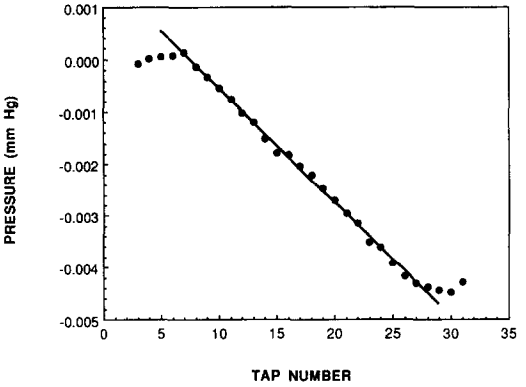

FIG. 6(a). Measured pressure distribution in a 90-deg vertex angle pin fin array for $Re = 44.8$. $S_T/W = 2.00$ and $S_L/W = 1.73$.

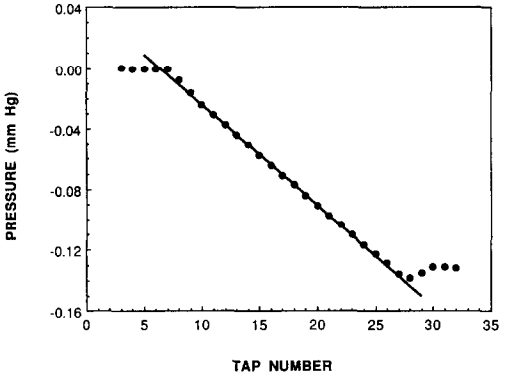

FIG. 5(b). Measured pressure distribution in a 45-deg vertex angle pin fin array for $Re = 378.6$. $S_T/W = 2.00$ and $S_L/W = 1.73$.

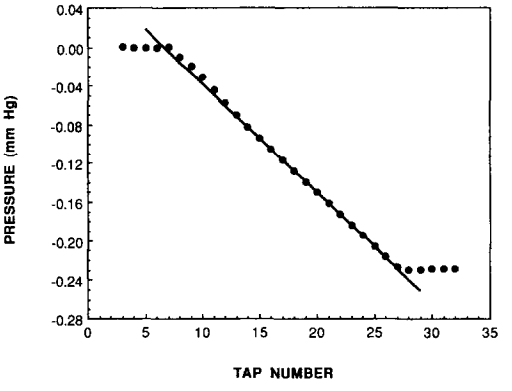

FIG. 6(b). Measured pressure distribution in a 90-deg vertex angle pin fin array for $Re = 381$. $S_T/W = 2.00$ and $S_L/W = 1.73$.

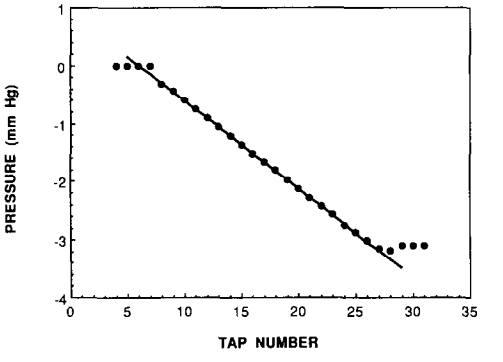

FIG. 5(c). Measured pressure distribution in a 45-deg vertex angle pin fin array for $Re = 2210$. $S_T/W = 2.00$ and $S_L/W = 1.73$.

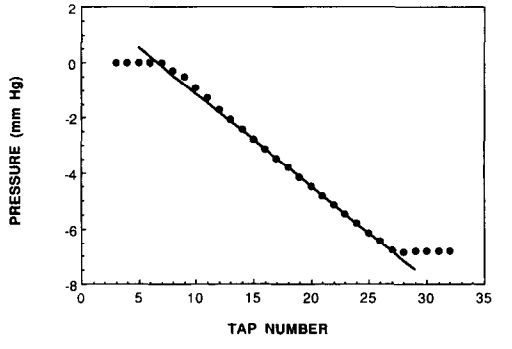

FIG. 6(c). Measured pressure distribution in a 90-deg vertex angle pin fin array for $Re = 2145$. $S_T/W = 2.00$ and $S_L/W = 1.73$.

An overall inspection of Figs. 5 and 6 reveals a slight scatter of the data in Figs. 5(a) and 6(a), which correspond to the low Re value of 45, while the data displayed in the other figures are remarkably free of scatter. From an examination of all of the data for all of the runs, it was noted that only for the two lowest Reynolds numbers, $Re \sim 20$ and 45, was there any evidence of data scatter. All of the other 25 runs were totally free of scatter, i.e. classic examples of excellent data.

The presence of scatter at the very low Re and its absence at larger Re is readily rationalized. At the very low Re, the pressure drop in the array is so small that the flow is affected by pressure fluctuations in the laboratory from which the air is drawn into the test section. Such fluctuations were caused, for example,

by the laboratory ventilation system. As the Reynolds number increased, the array pressure drop substantially exceeded the magnitude of the pressure fluctuations in the laboratory, so that the fluctuations no longer affected the flow.

The pressure distributions of Figs. 5 and 6 exhibit a common pattern. Upstream of the array, the pressure distribution is flat. Within the array (taps 8–27), the pressure decreases nearly linearly, with the only deviations from strict linearity being confined to the initial rows of the array. At the exit of the array, the flow may experience a slight pressure recovery as a result of the deceleration of the flow, after which the pressure distribution becomes flat downstream of the array.

The foregoing overview will now be supplemented by a more detailed commentary based not only on Figs. 5 and 6 but also on the other data runs not exhibited in the figures. The first issue has to do with the establishment of the periodic fully developed regime, where the flow pattern is precisely repeated from row to row. The attainment of this regime is evidenced by the axial invariance of Δp_{row}, i.e. by a linear decrease of the pressure at successive taps axially separated by S_L.

At low Reynolds numbers, the fully developed regime is attained after just one row of fins for both of the investigated fin geometries. As the Reynolds number increases, there is a marked difference in where the fully developed regime is respectively achieved for 45- and 90-deg vertex angle arrays. The pressure distributions for the 45-deg array continue to become fully developed after just one row of fins for the entire range of Reynolds numbers. Thus, there is virtually no hydrodynamic development length. However, for the 90-deg vertex angle fins at the higher Reynolds numbers, the fully developed pressure distribution is not attained until after five or six rows in the array. The substantially slower development for the 90-deg array can be attributed to its relative openness in contrast to the 45-deg array. In particular, the boundaries of a flow lane for the 90-deg array include a high proportion of symmetry line surface, which offers no constraint to the flow. On the other hand, for the 45-deg case, the lane boundaries are mostly solid surfaces, which constrain the flow and hasten its hydrodynamic development.

Another difference in the pressure distributions for the two fin geometries is the magnitude of the pressure recovery at the exit of the array. Although in neither case is the recovery appreciable, it is, at least, discernible for the 45-deg array, but hardly perceptible for the 90-deg array.

The dimensionless pressure coefficient ξ, which expresses the fully developed pressure drop per row, was evaluated from the experimental data in accordance with equation (1). The thus-determined ξ values are plotted in Fig. 7 as a function of the Reynolds number $Re = \rho V_{max} W/\mu$, with different symbols used to distinguish the results for the 45- and 90-deg vertex angle fin arrays. Both arrays are characterized by

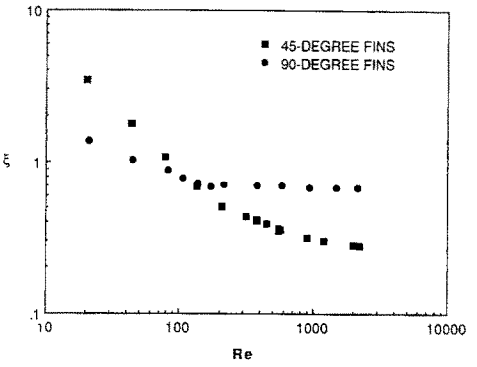

FIG. 7. Experimentally determined per-row pressure coefficients for 45- and 90-deg vertex angle pin fin arrays. $S_T/W = 2.00$ and $S_L/W = 1.73$.

$S_T/W = 2.00$ and $S_L/W = 1.73$ (staggered fin deployment on equilateral-triangular centers).

From the figure, it is seen that for both arrays, ξ displays its typical low-Reynolds-number behavior for staggered tube-bank arrays, i.e. ξ decreases with increasing Re, with the decrease becoming progressively more gradual. At larger Re, the ξ values for the 90-deg vertex angle array are independent of Re, while those for the 45-deg vertex angle array are tending toward independence. The flattening of the ξ–Re distribution is due to the increasing importance of the inertia-related losses relative to the friction-related losses. Owing to the relative openness of the 90-deg array, the inertial losses come to prominence earlier in that array than in the 45-deg array, thereby explaining the earlier leveling off of the data for the former.

At lower Re, where friction dominates, the ξ values for the 45-deg array are greater than those for the 90-deg array. At the larger Re, where inertia dominates, the opposite ordering is in evidence. These findings are in accord with the relative openness and the low presence of solid boundaries in the 90-deg case and with the relative tightness and the high presence of solid boundaries in the 45-deg case.

As outlined in Section 2.3, an attempt was made to deduce the entrance and exit losses by the differencing operation defined by equation (4) and discussed in the related text. Since small differences between relatively equal numbers are involved, the results are expected to display considerable scatter. This expectation was reflected in reality, as witnessed in Fig. 8, where the dimensionless entrance–exit pressure loss ϕ (equation (5)) is plotted as a function of the Reynolds number. To assist in identifying the data, the plotted points for each of the arrays have been interconnected with the straight line segments.

Despite the scatter, a significant conclusion can be drawn by comparing the magnitudes of ϕ with the magnitudes of ξ in Fig. 7. Such a comparison reveals that the entrance and exit losses are always less than the pressure drop in one row of the array in the fully developed regime. In particular, at low Reynolds numbers, the entrance and exit losses are substantially

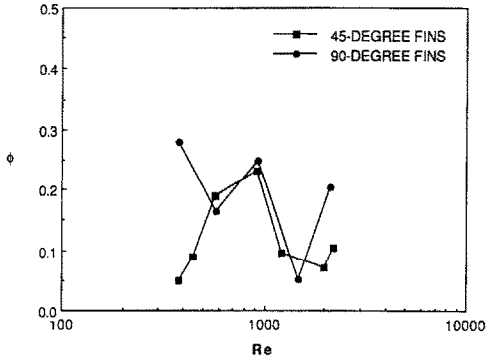

FIG. 8. Dimensionless combined entrance and exit pressure losses for 45- and 90-deg vertex angle pin fin arrays. $S_T/W = 2.00$ and $S_L/W = 1.73$.

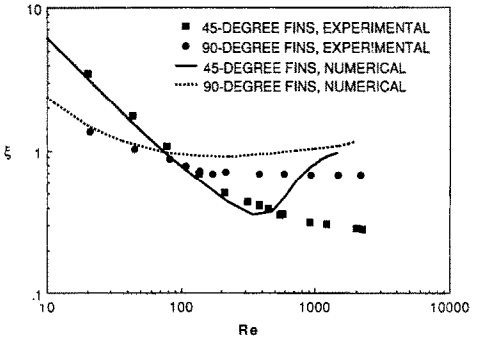

FIG. 9. Comparison of experimentally and numerically determined per-row pressure coefficients for 45- and 90-deg pin fin arrays. $S_T/W = 2.00$ and $S_L/W = 1.73$.

smaller than that for one row. This finding reinforces the practice of neglecting the entrance and exit losses for arrays in which there are more than 9 or 10 rows [2, 3].

4. DEVELOPMENT OF DESIGN EQUATIONS

In the preceding sections of the paper, highly accurate experimental results were reported for the pressure drop characteristics of selected diamond-shaped pin fin arrays. These results will be employed as a standard of comparison in a numerically based development aimed at providing design equations for determining the pressure drop characteristics of arrays characterized by a wide range of transverse and longitudinal spacings.

The numerical work, to be described elsewhere [1], encompassed solutions of the partial differential equations of mass and momentum for steady, laminar, constant-property flow. The fluid flow and pressure fields were modeled as being periodically fully developed, whereby the flow pattern is precisely repeated from row to row, and the pressure drop per row is axially unchanging. For the numerical implementation, the FIDAP general-purpose fluid dynamic code was employed. This is a finite-element code in which two-dimensional, nine-noded finite elements are used to discretize the solution domain. Supplementary computer runs were made to establish the number of elements needed for accurate solutions [1].

The first set of numerical solutions corresponded to the geometries and operating conditions of the experiments. These solutions yielded the dimensionless per-row pressure drop, represented by the pressure coefficient ξ of equation (1), as a function of the Reynolds number $Re = \rho V_{max} W/\mu$. The numerically and experimentally determined ξ vs Re distributions have been brought together in Fig. 9 for purposes of comparison.

From the figure, it is seen that the numerical predictions for the 45-deg pin fin array track the experimental data very well up to a Reynolds number of about 500. Beyond that point, the predicted ξ–Re distribution tilts upward and breaks away from the experimental data. The divergence may be due to various factors. One factor is that the laminar model may no longer be valid. Another possible factor is that the FIDAP representation of the inertial terms may not be appropriate for the vigorous recirculation which occurs at the larger Reynolds numbers, and similarly for the neglect of time dependencies.

For the 90-deg pin fin array, the close tracking of the experimental data by the predictions is confined to Reynolds numbers below 100. However, the predictions and the data are in qualitative agreement about the relative insensitivity of ξ to Re in the range of Re between 150 and 500. At $Re = 200$, the data are about 22% below the predictions, and at $Re = 500$, the data are about 27% below.

The lesser level of agreement for the 90-deg array compared with the 45-deg array can be rationalized by considering the same factors as were discussed in rationalizing the comparison between the predictions and the data for the 45-deg case. Since the 90-deg array is more open than its 45-deg counterpart, it may be subject to earlier laminar–turbulent transition, to more vigorous recirculation, and to greater unsteadiness.

The foregoing comparisons of numerical and experimental results lend strong encouragement for the use of the numerical simulation to predict the pressure drop characteristics for diamond-shaped pin fin arrays having other S_T and S_L array spacings. In particular, since almost all of the subsequent numerical work was performed for tighter arrays (smaller S_T and S_L) than those examined in Fig. 9, the accuracy of the numerical predictions is expected to be even better.

The array spacings for which numerical solutions were carried out are listed in Table 1. As seen in the table, consideration was given to arrays consisting of either 45- or 90-deg vertex angle diamond-shaped fins. The selected spacing ratios S_T/W and S_L/W correspond to either of two patterns of fin deployment—$S_L/W = 0.866(S_T/W)$ or S_T/W. The former is the equilateral triangular deployment, while the latter cor-

Table 1. Array spacings for the numerical solutions

S_T/W	S_L/W	S_T/W	S_L/W
(a) 45-deg vertex angle fins			
1.40	1.21	1.25	1.25
1.50	1.30	1.50	1.50
1.75	1.52	1.75	1.75
2.00	1.73	2.00	2.00
(b) 90-deg vertex angle fins			
1.15	1.00	1.15	1.15
1.25	1.08	1.25	1.25
1.35	1.17	1.50	1.50
1.50	1.30	2.00	2.00
1.75	1.52		
2.00	1.73		

responds to equal transverse and longitudinal spacings. All of the investigated arrays are of the staggered type.

For each of the arrays listed in Table 1, the dimensionless per-row pressure drop in the periodic fully developed region was determined as a function of the Reynolds number over a range similar to that of Fig. 9. To facilitate the application of these results to design, it is appropriate to seek an algebraic representation for them. Such a representation not only has the benefit of compactness, but it also can serve as a means of interpolation to obtain results for cases other than those for which the solutions were performed.

It was soon discovered that a single algebraic correlation of all of the results could not be obtained, so that separate correlations were sought for each of the four groupings in Table 1. Furthermore, in the search for the tightest possible correlations, it was found advantageous to explore other characteristic lengths as alternatives to the maximum fin width W. One of these was the perpendicular distance between parallel faces of neighboring diamond-shaped fins. The other was based on the porosity of the array. The latter generally proved advantageous, and it was utilized in the correlations.

The porosity-based characteristic dimension may be derived by treating the array as a packed bed. Then, following Whitaker [4]

$$D^* = 4\frac{\text{volume of bed available for flow}}{\text{wetted surface}}. \quad (7)$$

Since the array is modular, equation (7) may be evaluated for a typical module, with the result

$$D^* = 2(S_T S_L - WL/2)/(W^2+L^2)^{1/2}. \quad (8)$$

The Reynolds number based on D^* is

$$Re^* = \rho V_{max} D^*/\mu. \quad (9)$$

The initial correlations were structured as algebraic relations between the pressure coefficient ξ of equation (1) and Re^*. However, upon further consideration, it was realized that for the 45-deg vertex angle arrays, especially the tighter arrays, the flow passing along any lane through the array was very nearly a channel flow (i.e. the boundaries of the lane were, for the most part, solid boundaries). Therefore, it appeared reasonable to seek a correlation based on a channel-like friction factor, i.e.

$$f = [(\Delta p_{row}/S_L)D^*]/\tfrac{1}{2}\rho V_{max}^2. \quad (10)$$

Indeed, for the 45-deg arrays, f proved to be a better correlation parameter than ξ. On the other hand, for the 90-deg arrays, because of their relative openness, ξ was the better correlation parameter.

Taking guidance from the standard practice used for flow in porous media, a Forchheimer-type relationship was used to correlate the results, i.e.

$$y = C_1/Re^* + C_2 \quad (11)$$

where y is either f or ξ, and C_1 and C_2 were selected to best represent the results for all of the spacings in a given correlation group.

The correlations for the 45-deg vertex angle fin arrays will be presented first. For the $S_L/W = 0.866 \times (S_T/W)$ arrays of Table 1(a)

$$f = 108/Re^* + 0.088 \quad (12)$$

where the correlation is valid up to $Re^* = 200$. The correlation for the $S_L/W = S_T/W$ arrays of Table 1(a) is

$$f = 97/Re^* + 0.12 \quad (13)$$

for $Re^* \leqslant 100$.

The correlations for the 90-deg vertex angle fin arrays required separate representations for the range of smaller and larger S_T/W. For the $S_L/W = 0.866 \times (S_T/W)$ arrays of Table 1(b)

$$\xi = 127/Re^* + 0.90 \quad (14a)$$

$$\xi = 88/Re^* + 0.70 \quad (14b)$$

respectively for $S_T/D < 1.35$ and $S_T/D \geqslant 1.35$. These correlations are applicable for Re^* up to 500. For the $S_L/W = S_T/W$ arrays of Table 1(b), the correlations are

$$\xi = 155/Re^* + 0.82 \quad (15a)$$

$$\xi = 98/Re^* + 0.72 \quad (15b)$$

where the ranges of S_T/D and Re^* are the same as for equations (14a) and (14b).

5. CONCLUDING REMARKS

The research reported here is a synergistic blend of experimentation and numerical simulation directed toward the determination of the pressure drop characteristics of arrays of diamond-shaped pin fins. In the experimental portion of the investigation, highly accurate per-row pressure drop information was collected for specific pin fin arrays. These data served to validate a finite-element-based numerical simulation. Once the simulation model was verified, it was

employed to generate information for a wide range of array geometrical parameters, as set forth in Table 1.

To facilitate the use of the computer-generated pressure drop information in design, compact algebraic representations were developed. These formulas, conveyed by equations (12)–(15), served to relate the dimensionless per-row pressure drop in the hydrodynamically developed regime to the Reynolds number. For arrays consisting of diamond-shaped fins with a 45-deg vertex angle (Fig. 2), the channel-like nature of the flow passages prompted the use of a friction factor f similar to that used for conventional channel flows. On the other hand, the more open deployment which characterized the 90-deg vertex angle pin fin arrays motivated the use of the pressure coefficient ξ that is commonly used for conventional circular tube banks. The characteristic dimension appearing in both Re^* and f is based on the porosity of the array (equations (7) and (8)).

The experimental results, in addition to serving as a standard of comparison for the numerical simulation, provided information on the combined entrance and exit pressure losses and on the length of the hydrodynamic development region in the array. It was found that the entrance and exit losses were always less than the pressure drop per row in the hydrodynamically developed region of the array, especially at lower Reynolds numbers.

REFERENCES

1. V. B. Grannis and E. M. Sparrow, Numerical simulation of fluid flow through an array of diamond-shaped pin fins, *Numer. Heat Transfer*, Part A: *Applic.* (in press).
2. A. Zukauskas, Convective heat transfer in crossflow. In *Handbook of Single-phase Convective Heat Transfer*. Wiley, New York (1987).
3. E. S. Gaddis and V. Gnielinski, Pressure drop in cross flow across tube bundles, *Int. Chem. Engng* **25**, 1–14 (1985).
4. S. Whitaker, *Elementary Heat Transfer Analysis*, p. 223. Pergamon Press, Oxford (1976).

PERTE DE CHARGE DANS DES ECHANGEURS COMPORTANT DES ARRANGEMENTS D'AIGUILLES A TETE DE DIAMANT

Résumé—Des expériences et une simulation numérique sont faites pour déterminer les caractéristiques de perte de charge d'arrangements d'aiguilles à tête de diamant. Les paramètres géométriques S_T/W et S_L/W, où W est la largeur maximale de l'aiguille, S_T et S_L les espacements transverse et longitudinal, varient respectivement de 1,15 à 2,00 et de 1,00 à 2,00. Le nombre de Reynolds basé sur W et la vitesse maximale du fluide varie entre 20 et 2200. Par les expériences, on obtient des résultats précis de la perte de pression par rangée pour les pertes d'entrée et de sortie et pour la région de développement hydrodynamique. La perte de pression par rangée sert d'élément de comparaison pour les simulations numériques qui sont résolues par une méthode aux éléments finis appliquée au régime périodique complètement établi. Le modèle de simulation ainsi validé est employé pour fournir des résultats pour un large domaine de conditions géométriques. Pour faciliter l'application à des conceptions, les résultats de perte de charge par rangée sont unifiés par des formules algébriques compactes.

DRUCKABFALL IN WÄRMEÜBERTRAGERN, WELCHE AUS ANORDNUNGEN DIAMANTFÖRMIGER STIFTRIPPEN BESTEHEN

Zusammenfassung—Es wird eine breit angelegte Untersuchung zur Bestimmung des Druckabfalls von Anordnungen diamantförmiger Stiftrippen durchgeführt, welche ergänzende Versuche und numerische Lösungen einschließt. Die Geometrieparameter S_T/W und S_L/W liegen zwischen 1,15 und 2,0 bzw. 1,0 und 2,0, wobei W die maximale Rippenbreite, S_T und S_L die Quer- bzw. Längsteilung sind. Die untersuchten Rippen haben an der Vorderseite einen Scheitelwinkel von entweder 45 oder 90 Grad. Die mit der maximalen Rippenbreite und der maximalen Fluidgeschwindigkeit gebildete Reynolds-Zahl liegt zwischen 20 und 2200. Aus den Versuchen ergeben sich extrem genaue Ergebnisse für einzelne Anordnungen, und zwar für den Druckabfall je Reihe, für die kombinierten Eintritts- und Austrittsverluste sowie für die Länge des hydrodynamischen Anlaufgebiets. Die Ergebnisse für den Druckabfall je Reihe dienen als Vergleichsgrundlage für die numerischen Berechnungen, welche mit Hilfe eines Finite-Elemente-Verfahrens im periodisch vollständig entwickelten Gebiet ausgeführt worden sind. Das Simulationsmodell wird auf diese Weise zunächst validiert und anschließend für Berechnungen in einem weiten Bereich von geometrischen Bedingungen angewandt. Um die praktische Anwendung zu erleichtern, werden die numerisch berechneten Ergebnisse für den Druckabfall je Reihe mit Hilfe einer kompakten algebraischen Gleichung korreliert (Gleichungen (12) bis (15)).

ХАРАКТЕРИСТИКИ ПЕРЕПАДА ДАВЛЕНИЯ В ТЕПЛООБМЕННИКАХ, СОСТОЯЩИХ ИЗ НАБОРА РОБМОВИДНЫХ ИГОЛЬЧАТЫХ РЕБЕР

Аннотация—Проведено широкомасштабное исследование, включающее эксперименты и численное моделирование с целью определения характеристик перепада давления в наборах ромбовидных игольчатых ребер. Геометрические параметры наборов S_T/W и S_L/W изменялись соответственно от 1,15 до 2,00 и от 1,00 до 2,00, где W—максимальная ширина ребра, а S_T и S_L—поперечный и продольный шаги. Углы при вершине исследуемых ребер составляли 45 и 90 градусов. Число Рейнольдса, основанное на максимальной ширине ребра и максимальной скорости жидкости, изменялось в интервале от приблизительно 20 до 2200. Для выбранных наборов экспериментально получены достаточно точные данные по перепаду давления в единичном ряде ребер, совместным потерям на входе и выходе, а также по длине участка гидродинамического развития. Данные по перепаду давления в единичном ряде ребер используются в качестве стандарта для сравнения расчетов по численным моделям с применением метода конечных элементов к периодическому полностью развитому режиму. Апробированная таким образом модель используется для обобщения результатов, полученных для широкого диапазона геометрических условий. С целью облегчения применения при конструировании численные результаты по перепаду давления в единичном ряде ребер приведены в виде достаточно простых алгебраических уравнений (уравнения (12)–(15)).